Large eddy simulation of flow over an airfoil undergoing surging and pitching motions

Alexander Kocher
MS Student
Rensselaer Polytechnic Institute
Troy, NY, USA

Reed Cummings
Postdoctoral Associate
Rensselaer Polytechnic Institute
Troy, NY, USA

Onkar Sahni
Assistant Professor
Rensselaer Polytechnic Institute
Troy, NY, USA

ABSTRACT

A dynamic large eddy simulation (LES) approach is employed to study flow over an oscillating NACA 0018 airfoil with surging and pitching motions. Surging motion is studied at moderate and large advance ratios of λ=0.5 and 1.0, and a reduced frequency of k=0.0985. An airfoil at fixed incidence of 8° is set in a constant freestream flow at Reynolds number of Re_C=300,000. LES predictions for lift force are compared to experimental results at λ=0.5 and show a good agreement. LES predictions are also made at λ=1.0 which is at the tipping point of reverse flow regime. With a large surging amplitude, there is a loss of lift during the retreating phase, and a roll up and ejection of a distinct leading-edge vortex. Pitching motion is studied at Re_C=250,000 and k=0.074 with both mean and amplitude of incidence set to 10°. Again, LES predictions for lift force are compared with experiments. Unsteady Reynolds-averaged Navier-Stokes (URANS) predictions are also made. LES predictions show similar features in the force response as experiments while URANS lack few prominent features. In all cases, instantaneous flowfield is analyzed at different phases.

INTRODUCTION

Rotorcraft blades often experience unsteady flow conditions that affect the efficiency and capabilities of the flight. Two such examples are dynamic stall and reverse flow. In a forward flight, dynamic stall occurs due to cyclic pitching as the blade rotates along the azimuth. The result is a temporary increase in lift followed by a loss of lift with an increase in drag. Similarly, a reverse flow region appears in which the geometric trailing edge becomes the aerodynamic leading edge. With these phenomena coupled, the velocity of the forward flight gets limited and the blades experience additional fatigue.

Some of the recent work to understand these flow phenomena has been done by conducting experiments in a quasi-3D environment by subjecting a blade model to cyclic surging and/or pitching motions. Greenblatt et al. 1 looked into the effects of fluctuating freestream velocity and cyclic pitching on an airfoil section through experiments. Granlund et al. 2 considered the effect of large streamwise oscillations including a reverse flow regime, for different reduced frequencies, through water tunnel experiments. Numerical simulations have also been used as an effective way to further understand these effects. Numerical investigations on a quasi-3D model include that of Visbal 3 and Gross and Wen 4, with a high-order finite difference based large eddy simulation (LES), and Strangfeld 5, with unsteady Reynolds-averaged Navier-Stokes (URANS) simulations. Hodara et al. 6 investigated a pitching airfoil in a constant reverse flow (leading to a reserve dynamic stall) through a joint wind tunnel testing and numerical simulation based on a hybrid RANS-LES approach. Others have chosen to study the entire rotor in a forward flight using experimental testing (Ref. 7) or a RANS or hybrid RANS-LES approach, e.g., see (Refs. 8, 9).

In this study, a finite element (FE) based LES is used to study flow over a blade section undergoing surging and pitching motions. LES is an attractive methodology since it is tractable from a computational viewpoint as well as sufficiently accurate. On the other hand, URANS-based approach, or even hybrid RANS-LES approach, often leads to an inaccurate prediction, especially for complex flow conditions such as dynamic stall and reverse flow, while a direct numerical simulation (DNS) is often computationally prohibitive for complex problems of interest.

Current cases involve turbulent flows with a significant spatial and temporal inhomogeneity and thus, in LES we employ a dynamic procedure suitable for unstructured meshes based on a localized version of the variational Germano identity (VGI) (Refs. 10, 11). Further, the ease with which the FE method can be applied on unstructured meshes makes it a useful option for investigating many challenging problems of interest. Additionally, the adaptive meshing (Refs. 12–14), high-order (Refs. 15, 16), and parallelization (Refs. 17–19) capabilities of the FE method can significantly increase the computational efficiency.

Current LES is based on the experiments of a blade model

Presented at the AHS International 73rd Annual Forum & Technology Display, Fort Worth, Texas, USA, May 9–11, 2017.

composed of the NACA 0018 airfoil section subjected to unsteady conditions related to surging and pitching. In a surging (only) case, airfoil oscillates in the streamwise direction at a fixed incidence angle, where different sectional advacne ratios are considered including a value of 1.0 which is at the tipping point of reserve flow regime. In a pitching (only) case, incidence angle varies cyclically about a mean. A combined case includes both the surging and pitching motions. In this study, we consider surging (only) cases at two advance ratios (one moderate and one large), and a pitching (only) case with a large variation in incidence angle.

NUMERICAL METHODOLOGY

A dynamic LES methodology is currently employed. It uses a combined subgrid-scale model which is based on the residual-based variational multiscale (RBVMS) model along with the dynamic Smagorinsky eddy-viscosity model (Refs. 10,11,20). The dynamic procedure is local in nature and is based on a localized version of the variational Germano identity (Refs. 10, 11). In this procedure, Lagrangian averaging along fluid pathtubes is applied to make it robust while maintaining the localized nature of the VGI. Further, an arbitrary Lagrangian Eulerian (ALE) description is used to account for the deforming mesh due to the relative motion of the airfoil (Ref. 21).

Combined Model Formulation

This work uses the incompressible Navier Stokes equations in the arbitrary Lagrangian Eulerian (ALE) description. The strong form of the equations is given as

$$\begin{aligned} &u_{k,k} = 0 \\ &u_{i,t} + (u_j - u_j^m)u_{i,j} = -p_{,i} + \tau^v_{ij,j} + f_i \end{aligned} \tag{1}$$

where u_i is the velocity vector, u_i^m is the mesh velocity vector, p is the pressure (scaled by the constant density), $\tau^v_{ij} = 2\nu S_{ij}$ is the symmetric (Newtonian) viscous stress tensor (scaled by the density), ν is the kinematic viscosity, $S_{ij} = 0.5(u_{i,j} + u_{j,i})$ is the strain-rate tensor, and f_i is the body force vector (per unit mass). Note that Einstein summation notation is used.

The weak form is stated as follows: find $\mathbf{u} \in \mathscr{S}$ and $p \in \mathscr{P}$ such that

$$\begin{aligned} B(\{w_i,q\},\{u_i,p\};u_l^m) = &\int_\Omega [w_i(u_{i,t} + u_i u^m_{j,j}) \\ &+ w_{i,j}(-u_i(u_j - u_j^m) + \tau^v_{ij} - p\delta_{ij}) \\ &- q_{,k}u_k]\, d\Omega \\ &+ \int_{\Gamma_h} [w_i(u_i(u_j - u_j^m) - \tau^v_{ij} + p\delta_{ij})n_j \\ &+ q u_k n_k]\, d\Gamma_h \\ &= \int_\Omega w_i f_i d\Omega \end{aligned} \tag{2}$$

for all $\mathbf{w} \in \mathscr{W}$ and $q \in \mathscr{P}$. $\mathscr{S}$ and $\mathscr{P}$ are suitable trial/solution spaces and $\mathscr{W}$ is the test/weight space. $\mathbf{w}$ and q are the weight functions for the velocity and pressure variables, respectively. Ω is the spatial domain and Γ_h is the portion of the domain boundary with Neumann or natural boundary conditions.

The above weak form can be written concisely as: find $\boldsymbol{U} \in \mathscr{U}$ such that

$$B(\boldsymbol{W},\boldsymbol{U};u_l^m) = (\boldsymbol{W},\boldsymbol{F}) \tag{3}$$

for all $\boldsymbol{W} = [\mathbf{w},q]^T \in \mathscr{V}$. $\boldsymbol{U} = [\mathbf{u},p]^T$ is the vector of unknown solution variables and $\boldsymbol{F} = [\mathbf{f},0]^T$ is the source vector. The solution and weight spaces are: $\mathscr{U} = \{\boldsymbol{U} = [\mathbf{u},q]^T | \mathbf{u} \in \mathscr{S}; p \in \mathscr{P}\}$ and $\mathscr{V} = \{\boldsymbol{W} = [\mathbf{w},q]^T | \mathbf{w} \in \mathscr{W}; q \in \mathscr{P}\}$, respectively.

Throughout this text $B(\cdot,\cdot)$ is used to represent the semi-linear form that is linear in its first argument and $(\cdot,\cdot)$ is used to denote the L_2 inner product. $B(\boldsymbol{W},\boldsymbol{U};u_l^m)$ is split into bilinear and semi-linear terms as shown below.

$$B(\boldsymbol{W},\boldsymbol{U};u_l^m) = B_1(\boldsymbol{W},\boldsymbol{U};u_l^m) + B_2(\boldsymbol{W},\boldsymbol{U}) = (\boldsymbol{W},\boldsymbol{F}) \tag{4}$$

where $B_1(\boldsymbol{W},\boldsymbol{U};u_l^m)$ contains the bilinear terms and $B_2(\boldsymbol{W},\boldsymbol{U})$ consists of the semi-linear terms. These are defined as

$$\begin{aligned} B_1(\boldsymbol{W},\boldsymbol{U};u_l^m) = &\int_\Omega [w_i(u_{i,t} + u_i u^m_{j,j}) \\ &+ w_{i,j}(u_i u_j^m + \tau^v_{ij} - p\delta_{ij}) - q_{,k}u_k]\, d\Omega \\ &+ \int_{\Gamma_h} [w_i(-u_i u_j^m - \tau^v_{ij} + p\delta_{ij})n_j + q u_k n_k]\, d\Gamma_h \end{aligned} \tag{5}$$

$$B_2(\boldsymbol{W},\boldsymbol{U}) = -\int_\Omega w_{i,j}u_i u_j d\Omega + \int_{\Gamma_h} w_i u_i u_j n_j d\Gamma_h \tag{6}$$

The Galerkin weak form is obtained by considering the finite-dimensional or discrete solution spaces $\mathscr{S}^h \subset \mathscr{S}$ and $\mathscr{P}^h \subset \mathscr{P}$ and the weight space $\mathscr{W}^h \subset \mathscr{W}$, where the superscript h is used as a mesh parameter to denote discretized spaces and variables in a finite element context. Using these spaces, $\mathscr{U}^h = \{\boldsymbol{U}^h = [\mathbf{u}^h,p^h]^T | \mathbf{u}^h \in \mathscr{S}^h; p^h \in \mathscr{P}^h\}$ and $\mathscr{V}^h = \{\boldsymbol{W}^h = [\mathbf{w}^h,q^h]^T | \mathbf{w}^h \in \mathscr{W}^h; q^h \in \mathscr{P}^h\}$ are defined. The Galerkin weak form is then stated concisely as: find $\boldsymbol{U}^h \in \mathscr{U}^h$ such that

$$B(\boldsymbol{W}^h,\boldsymbol{U}^h) = (\boldsymbol{W}^h,\boldsymbol{F}) \tag{7}$$

for all $\boldsymbol{W}^h \in \mathscr{V}^h$. Note for brevity we have dropped u_l^m term. The Galerkin weak formulation corresponds to a method for direct numerical simulation since no modeling is employed. However, when the finite-dimensional spaces are incapable of representing the fine/small scales, the Galerkin formulation yields an inaccurate solution. A model term is added to overcome this difficulty, e.g., as done in the residual-based variational multiscale (RBVMS) formulation.

In RBVMS, a set of model terms is added to the Galerkin weak form that results in the following variational formulation: find $\boldsymbol{U}^h \in \mathscr{U}^h$ such that

$$B(\boldsymbol{W}^h,\boldsymbol{U}^h)+M_{rbvms}(\boldsymbol{W}^h,\boldsymbol{U}^h)=(\boldsymbol{W}^h,\boldsymbol{F}) \tag{8}$$

for all $\boldsymbol{W}^h \in \mathscr{V}^h$. M_{rbvms} represents the set of model terms due to the RBVMS approach.

A scale separation is used to decompose the solution and weight spaces as $\mathscr{S}=\mathscr{S}^h \oplus \mathscr{S}'$ and $\mathscr{P}=\mathscr{P}^h \oplus \mathscr{P}'$, and $\mathscr{W}=\mathscr{W}^h \oplus \mathscr{W}'$, respectively. Thus, the solution and weight functions are decomposed as $u_i = u_i^h + u_i'$ and $p = p^h + p'$ or $\boldsymbol{U} = \boldsymbol{U}^h + \boldsymbol{U}'$, and $w_i = w_i^h + w_i'$ and $q = q^h + q'$ or $\boldsymbol{W} = \boldsymbol{W}^h + \boldsymbol{W}'$, respectively. Note that coarse-scale or resolved quantities are denoted by $(\cdot)^h$ and fine-scale or unresolved quantities by $(\cdot)'$. The coarse-scale quantities are resolved by the grid whereas the effects of the fine scales on the coarse scales are modeled. In RBVMS, the fine scales are modeled as a function of the strong-form residual due to the coarse-scale solution. This is represented abstractly as $\boldsymbol{U}' = \mathscr{F}(\boldsymbol{R}(\boldsymbol{U}^h);\boldsymbol{U}^h)$, where $\boldsymbol{R}(\cdot)=[\boldsymbol{R}^m(\cdot),R^c(\cdot)]^T$ is the strong-form residual of the equations with $\boldsymbol{R}^m(\cdot)$ (or $R_i^m(\cdot)$) and $R^c(\cdot)$ as those of the momentum and continuity equations, respectively. Specifically, the fine-scale quantities are modeled as $u_i' \approx -\tau_M R_i^m(u_k^h,p^h;u_l^m)$ and $p' \approx -\tau_C R^c(u_k^h)$, where τ_C and τ_M are stabilization parameters (e.g., see details in Tran and Sahni (Refs. 11, 20)). This provides a closure to the coarse-scale problem as it involves coarse-scale solution as the only unknown. This is why $M_{rbvms}(\boldsymbol{W}^h,\boldsymbol{U}^h)$ is written only in terms of the unknown coarse-scale solution $\boldsymbol{U}^h$. In summary, $M_{rbvms}(\boldsymbol{W}^h,\boldsymbol{U}^h)$ can be written as

$$\begin{aligned}
M_{rbvms}(\boldsymbol{W}^h,\boldsymbol{U}^h) = \\
\sum_e \int_{\Omega_e^h} [& \underbrace{-(w_i^h u_{j,j}^m + w_{i,j}^h u_j^m)\tau_M R_i^m(u_k^h,p^h;u_l^m)}_{M^{ALE}_{rbvms}(\boldsymbol{W}^h,\boldsymbol{U}^h)} \\
& + \underbrace{q_{,i}^h \tau_M R_i^m(u_k^h,p^h;u_l^m)}_{M^{cont}_{rbvms}(\boldsymbol{W}^h,\boldsymbol{U}^h)} + \underbrace{w_{i,j}^h \tau_C R^c(u_k^h)\delta_{ij}}_{M^{P}_{rbvms}(\boldsymbol{W}^h,\boldsymbol{U}^h)} \\
& + \underbrace{w_{i,j}^h \left(u_i^h \tau_M R_j^m(u_k^h,p^h;u_l^m) + \tau_M R_i^m(u_k^h,p^h;u_l^m) u_j^h \right)}_{M^{C}_{rbvms}(\boldsymbol{W}^h,\boldsymbol{U}^h)} \\
& \underbrace{- w_{i,j}^h \tau_M R_i^m(u_k^h,p^h;u_l^m)\tau_M R_j^m(u_k^h,p^h)}_{M^{R}_{rbvms}(\boldsymbol{W}^h,\boldsymbol{U}^h)}] d\Omega_e^h
\end{aligned} \tag{9}$$

Note that all model terms are written in terms of the resolved scales within each element (where e denotes an element and contributions from all elements are summed). The last model term is used to represent the Reynolds stresses (i.e., M^R_{rbvms}) while the two terms prior to it are used to represent the cross-stress terms (i.e., M^C_{rbvms}).

In previous studies (Refs. 11, 22), it was found that the RBVMS model provides a good approximation for the turbulent dissipation due to the cross stresses but the dissipation due to the Reynolds stresses is underpredicted and turns out to be insufficient. Therefore, a combined subgrid-scale model was employed which uses the RBVMS model for the cross-stress terms and the dynamic Smagorinsky eddy-viscosity model for the Reynolds stress terms. This was done in both a finite element code (Refs. 10, 11) and a spectral code (Ref. 22). The combined subgrid-scale model is defined as

$$B(\boldsymbol{W}^h,\boldsymbol{U}^h)+M_{comb}(\boldsymbol{W}^h,\boldsymbol{U}^h;C_S,h)=(\boldsymbol{W}^h,\boldsymbol{F}) \tag{10}$$

where

$$\begin{aligned}
M_{comb}(\boldsymbol{W}^h,\boldsymbol{U}^h;C_S,h) = & M^{ALE}_{rbvms}(\boldsymbol{W}^h,\boldsymbol{U}^h)+M^{cont}_{rbvms}(\boldsymbol{W}^h,\boldsymbol{U}^h) \\
& + M^{P}_{rbvms}(\boldsymbol{W}^h,\boldsymbol{U}^h)+M^{C}_{rbvms}(\boldsymbol{W}^h,\boldsymbol{U}^h) \\
& + (1-\gamma)M^{R}_{rbvms}(\boldsymbol{W}^h,\boldsymbol{U}^h) \\
& + \gamma M^{R}_{smag}(\boldsymbol{W}^h,\boldsymbol{U}^h;C_S,h)
\end{aligned} \tag{11}$$

$$M^R_{smag}(\boldsymbol{W}^h,\boldsymbol{U}^h;C_S,h)=\int_\Omega w_{i,j}^h 2 \underbrace{(C_S h)^2|S^h|}_{\nu_t} S_{ij}^h d\Omega \tag{12}$$

where ν_t is the eddy viscosity, $|S^h|$ is the norm of the strain-rate tensor (i.e., $|S^h|=\sqrt{2\boldsymbol{S}^h:\boldsymbol{S}^h}=\sqrt{2S_{ij}^h S_{ij}^h}$), h is the local mesh size, and C_S is the Smagorinsky parameter. The parameter γ is set to be either 0 or 1 in order to control which model is used for the Reynolds stresses. Note that $\gamma=0$ results in the original RBVMS model and $\gamma=1$ results in the combined subgrid-scale model. In the current study, both values of γ resulted in similar predictions (which is expected due to use of a sufficiently fine mesh in each case as discussed in the next section). The Smagorinsky parameter is computed dynamically in a local fashion as discussed below.

Dynamic Procedure

To dynamically compute the Smagorinsky parameter in a local fashion, we follow the localized version of the variational Germano identity (VGI) developed by Tran *et al.* (Refs. 10, 11). In this procedure, Lagrangian averaging along fluid pathtubes is applied to make it robust and which maintains the localized nature of the VGI. The dynamic local procedure and the associated approximations are summarized in this section.

Local Variational Germano Identity The VGI involves comparing the variational form (including the model terms) between different levels of the discretization such that they are nested. In the localized version of the VGI, a set of nested spaces are constructed by using a series of coarser second-level grids along with the primary or original grid. We refer to the primary grid as the h-grid and any grid in the series of second-level grids as the H-level grid. Each H-level grid is

chosen such that it is associated with an interior node in the primary grid. This is done such that each H-grid is identical to the h-grid except that the given node k in the h-grid is coarsened or removed resulting in a nested H-level grid for node k, which we refer to as the H_k-grid. Note that each H_k-grid involves local coarsening around a given node k while the remainder of the mesh remains the same. This is demonstrated in 1-D in Figure 1, where Ω^{H_k} is the macro element in the H_k-grid corresponding to node k while Ω^{P_k} is the corresponding patch of elements around node k in the h-grid. Note that $k = 1, 2, \ldots, n_{intr}$, where n_{intr} is the number of interior nodes in the h-grid. Therefore, there are n_{intr} grids at the H level, each of which is paired with the primary h-grid. This results in the following spaces for each interior node, $\mathscr{U}^{H_k} \subset \mathscr{U}^h \subset \mathscr{U}$ and $\mathscr{V}^{H_k} \subset \mathscr{V}^h \subset \mathscr{V}$, for the solution and weight functions, respectively.

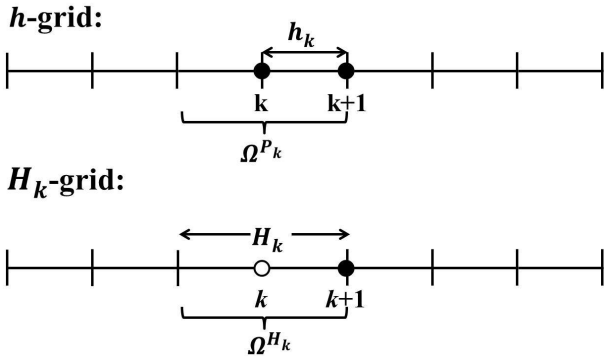

Fig. 1: 1-D schematic of the h- and H-level grids for local VGI

The local VGI procedure then uses the H_k-grids with the h-grid to compute the model parameter at every node k in the h-grid. By setting $\boldsymbol{W}^h = \boldsymbol{W}^{H_k}$, since $\mathscr{V}^{H_k} \subset \mathscr{V}^h \subset \mathscr{V}$, we get (for details see Ref. 11).

$$M_{comb}(\boldsymbol{W}^{H_k}, \boldsymbol{U}^h; C_S^k, h_k) - M_{comb}(\boldsymbol{W}^{H_k}, \boldsymbol{U}^{H_k}; C_S^k, H_k) = -(B(\boldsymbol{W}^{H_k}, \boldsymbol{U}^h) - B(\boldsymbol{W}^{H_k}, \boldsymbol{U}^{H_k})) \tag{13}$$

We recognize that determining $\boldsymbol{U}^{H_k}$ for each interior node k involves a grid-level computation or projection (operations which involve looping over the elements of the H_k-grid). This is prohibitive and therefore, a surrogate is considered. $\boldsymbol{U}^{H_k}$ is approximated within the macro element using a volume-weighted average of $\boldsymbol{U}^h$ while outside of the macro element the solution is assumed to be the same between the two grid levels. This assumption further bypasses a grid-level computation. This assumption arises from the requirement on the variational multiscale (VMS) method to provide element-level localization and the desire to yield nodal exactness at element corners (Ref. 23). This leads to $\boldsymbol{U}^{H_k} \approx \widetilde{\boldsymbol{U}}^{H_k}|_{\Omega^{H_k}} = \mathbb{A}^{H_k}(\boldsymbol{U}^h)$, where $\mathbb{A}^{H_k}$ is the local averaging operator defined below.

$$\mathbb{A}^{H_k}(f^h) = \frac{1}{|\Omega^{P_k}|} \int\limits_{\Omega_e^h \in \Omega^{P_k}} f^h d\Omega_e^h \tag{14}$$

where $|\Omega^{P_k}|$ is the volume of the local patch and Ω_e^h indicates an element in the h-grid.

This choice is only feasible when the spatial derivatives exist on the weight function. Furthermore, instead of using $\widetilde{\boldsymbol{U}}^{H_k}$ to compute $\boldsymbol{S}^{H_k}$, $\boldsymbol{S}^{H_k}$ is also approximated within the macro element as $\widetilde{\boldsymbol{S}}^{H_k}|_{\Omega^{H_k}} \approx \mathbb{A}^{H_k}(\boldsymbol{S}^h)$. Furthermore, among all of the terms in Equation (13) not involving the unknown model parameter, the non-linear convective term is found to be dominating (Refs. 10, 11). We note that this assumption holds exactly in a spectral setting where all the bilinear terms cancel out between the H- and h-level grids due to the L_2 orthogonality of spectral modes (Ref. 24). The local VGI simplifies to

$$-(B_2(\boldsymbol{W}^{H_k}, \boldsymbol{U}^h)_{\Omega^{P_k}} - B_2(\boldsymbol{W}^{H_k}, \widetilde{\boldsymbol{U}}^{H_k})_{\Omega^{H_k}} \\ M_{smag}(\boldsymbol{W}^{H_k}, \boldsymbol{U}^h; C_S^k, h_k)_{\Omega^{P_k}} - M_{smag}(\boldsymbol{W}^{H_k}, \widetilde{\boldsymbol{U}}^{H_k}; C_S^k, H_k)_{\Omega^{H_k}} \tag{15}$$

Now an appropriate choice for $\boldsymbol{W}^{H_k} \in \mathscr{V}^{H_k}$ must be made. In a 1D setting, we select $\boldsymbol{W}^{H_k} = [w_i^{H_k}, 0]^T$ with $w_i^{H_k}$ such that it is linear along a spatial direction within the macro element and is constant or flat outside. Within the macro element, $w_i^{H_k}$ is selected such that

$$w_{i,j}^{H_k} = \frac{1}{\prod_{j=1}^{N} (H_k)_j} = \frac{1}{|\Omega^{H_k}|} \tag{16}$$

where $(H_k)_j$ is the element length along the j^{th} direction and $|\Omega^{H_k}|$ is the volume of the element. Such a choice of $\boldsymbol{W}^{H_k}$ is also feasible in a multi-D setting and on an unstructured mesh consisting elements of mixed topology, however, a larger patch must be considered. An extra layer of elements is needed around the macro element to attain a constant value in the outside region. This extra layer acts as a buffer region. This choice is made due to its ease of implementation. For more details see Refs. 10, 11.

Local VGI Computation At this point we drop the subscript k in H_k and P_k and superscript k in C_S^k for brevity and only use it when necessary. The residual of the local VGI is defined as

$$\varepsilon_{ij} = L_{ij} - 2(C_S h)^2 M_{ij} \tag{17}$$

where

$$L_{ij} = \left(\left(\frac{1}{|\Omega^H|}, u_i^h u_j^h \right)_{\Omega^P} - \left(\frac{1}{|\Omega^H|}, \widetilde{u}_i^H \widetilde{u}_j^H \right)_{\Omega^H} \right) \tag{18}$$

$$M_{ij} = \left(\left(\frac{1}{|\Omega^H|}, |S^h| S_{ij}^h \right)_{\Omega^P} - \left(\frac{H}{h} \right)^2 \left(\frac{1}{|\Omega^H|}, |\widetilde{S}^H| \widetilde{S}_{ij}^H \right)_{\Omega^H} \right) \tag{19}$$

The least squares method is applied to determine the model parameter as follows

$$(C_S h)^2 = \frac{1}{2}\frac{L_{ij}M_{ij}}{M_{ij}M_{ij}} \tag{20}$$

Since the local VGI procedure often leads to negative values for $(C_S h)^2$, an averaging scheme is employed to avoid this issue. Specifically, Lagrangian averaging is applied (Ref. 25). To do so, two additional advection-relaxation scalar equations are solved. These are shown in Equations (21) and (22). The scalars I_{LM} and I_{MM} in these equations are the Lagrangian-averaged counterparts of $L_{ij}M_{ij}$ and $M_{ij}M_{ij}$, respectively.

$$I_{LM,t} + (u_j - u_j^m)I_{LM,j} = \frac{1}{T}(L_{ij}M_{ij} - I_{LM}) \tag{21}$$

$$I_{MM,t} + (u_j - u_j^m)I_{MM,j} = \frac{1}{T}(M_{ij}M_{ij} - I_{MM}) \tag{22}$$

where T is the timescale over which averaging is applied. Additionally, a local volume-weighted averaging is also applied separately to the numerator and denominator of Equation (20) as follows

$$(C_S h)^2 = \frac{1}{2}\frac{\mathbb{A}^H(I_{LM})}{\mathbb{A}^H(I_{MM})} \tag{23}$$

where, as before, $\mathbb{A}^H$ represents a local averaging operator. This is equivalent to averaging over local pathtubes (Refs. 10, 11) and maintains the utility of the local VGI.

Problem Setup and Discretization

This work considers oscillatory motion of a NACA 0018 airfoil. Two different types of cases are considered. In one type of case, the airfoil undergoes a sinusoidal surging motion (i.e., in the streamwise direction) at a fixed incidence angle in a constant freestream flow at a given (mean) chord-based Reynolds number. Two (sectional) advance ratios are considered. The other type of case considers an airfoil undergoing a sinusoidal pitching motion in a constant freestream or at a fixed Reynolds number.

Reynolds number is defined as $Re_C = U_\infty C/\nu$, where U_∞ is the freestream velocity and C is the chord length of the airfoil. For the surging cases, mean Reynolds number is 300,000, reduced frequency is 0.0985 and incidence angle is 8°. This is selected to match with the wind tunnel experiments of Ref. 26. The advance ratio is set to be 0.5 and 1.0, where 0.5 corresponds to a moderate value that is considered in the experiments and 1.0 falls in the high range and is at the tipping point of the reverse flow regime. In the pitching case, Reynolds number is 250,000, reduced frequency is 0.074 and mean incidence angle is 10° with an amplitude of 10°. Again, this is selected to match with the wind tunnel experiments of Ref. 27. All cases are summarized in Table 1.

In LES of the surging cases, displacement of the airfoil is defined as

Table 1: Summary of Cases

Case	Motion	λ	α	Re_c	k
Case 1	Surging	0.5	8°	300,000	0.0985
Case 2	Surging	1.0	8°	300,000	0.0985
Case 3	Pitching		10° ± 10°	250,000	0.074

$$d_{airfoil} = A\cos(2\pi ft) = A\cos(2\pi t/T) = A\cos(2\pi\tilde{t}) \tag{24}$$

where $T = 1/f$ is the time period. The variable $\tilde{t}$ is the fractional part in the oscillation cycle and is defined as $\tilde{t} = \{t/T\} = t/T - \lfloor t/T \rfloor$ (where $\lfloor\cdot\rfloor$ is the floor function). The reduced frequency is defined as $k = \pi f C/U_\infty$.

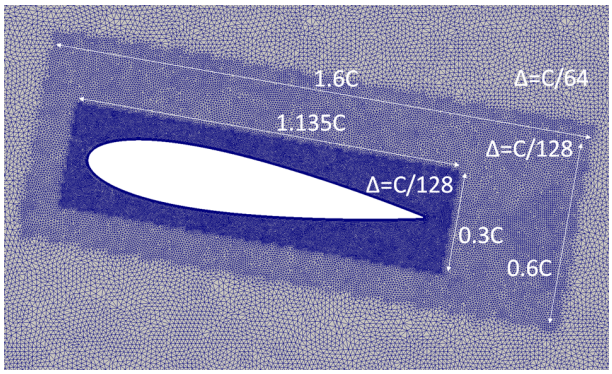

Fig. 2: Mesh with refinement zones around the airfoil at 10° (a similar mesh is used at 8°)

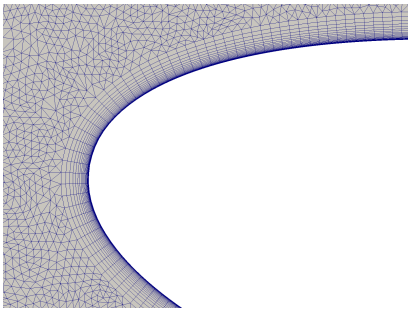

(a) Leading edge

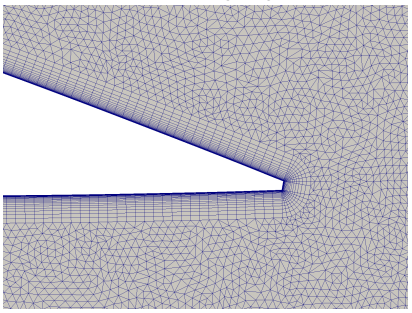

(b) Trailing edge

Fig. 3: Layered and graded mesh around the airfoil

The amplitude of is defined as

$$A = \frac{\lambda c}{2k} \tag{25}$$

where λ is the sectional advance ratio. The relative velocity is expressed as

$$U = U_\infty - U_{airfoil} = U_\infty(1 + \lambda sin(2\pi\tilde{t})) \tag{26}$$

At $\tilde{t}$=0, or ϕ=0° (phase in oscillation cycle), the airfoil velocity is zero and thus, the relative velocity is the freestream velocity. The same holds at $\tilde{t}$=0.5 or 180°. At $\tilde{t}$=0.25 or ϕ=90°, the airfoil is at the maximum relative velocity and at $\tilde{t}$=0.75 or ϕ=270° at the minimum relative velocity.

Similarly, the incidence angle of the airfoil is defined as

$$\alpha = \alpha_{mean} + \alpha_{amp} sin(\phi) = \alpha_{mean} + \alpha_{amp} cos(2\pi\tilde{t}) \tag{27}$$

where α_{mean} is the mean incidence angle and α_{amp} is the amplitude of incidence angle variation. At $\tilde{t}$=0 (ϕ=0°) and $\tilde{t}$=0.5 (ϕ=180°), the airfoil is at the mean incidence angle, while $\tilde{t}$=0.25 (ϕ=90°) and $\tilde{t}$=0.75 (ϕ=270°) correspond to the phases where the airfoil is at the maximum and minimum incidence angle, respectively.

The computational domain is set to be 100C x 50C x 0.2C. At the inlet, constant freestream velocity is applied. In surging cases, the airfoil is moved sinusoidally in the streamwise direction. Similarlly, to create a pitching motion, the airfoil is rotated sinusoidally about the quarter-chord. No-slip condition is prescribed on the airfoil surface. Slip condition is set at the top and bottom surfaces/walls. Side surfaces are imposed to be periodic. A natural pressure condition is used at the outlet. A second-order implicit time integration scheme, e.g., see (Ref. 11), is employed with about 1,440 steps in an oscillation cycle.

An unstructured mixed mesh (with hex and wedge elements) is used. An extrusion with 50 layers is applied in the spanwise direction. A layered and graded mesh is used around the airfoil surface, see Figures 3a and 3b. The first layer height is set to be $\mathcal{O}(10^{-5}C)$ and a geometric growth is applied to about 27 layers with a growth rate of 1.2. In each case, mesh is designed such that near-surface resolution of Δs^+, Δn^+ and Δz^+ (in wall units) along the streamwise, wall-normal and spanwise directions is set to be below 80, 1 and 50, respectively. Refinement zones are placed around the airfoil to resolve the flow structures of interest, see Figure 2 (where refinement zones are noted). The mesh is comprised of about 6.4 million nodes and 8.5 million elements in total. The computations were carried out using up to 4,096 cores of the IBM BlueGene/Q supercomputer available at Rensselaer's Center for Computational Innovations (CCI).

RESULTS AND DISCUSSION

In the following, we present LES predictions for the lift force and flowfield for both surging and pitching cases.

Surging - Force Response

Normalized lift (L/L_0, where L_0 is the lift of the static airfoil) is shown in Figure 4. In this figure, LES predictions are compared to the experimental data (Ref. 26) at an advance ratio of 0.5. LES predictions are also made for an advance ratio of 1.0. We further note that the LES data is instantaneous (i.e., taken over a single cycle) and therefore, exhibits fluctuations due to the presence of a turbulent flow over the airfoil; phase-averaged data from simulations will be considered in the future. For each advance ratio, LES is carried out for up to three oscillation cycles and data is presented from the last cycle.

Overall, there is reasonable agreement between the current LES predictions and experimental data. A high lift is observed at $\tilde{t}$=0.25 when the relative velocity is at its maximum (in the middle the advancing phase) while the lift is about minimum at $\tilde{t}$=0.75 (in the middle of the retreating phase). The overall temporal profile follows a variation that is proportional to the square of relative velocity (or instantaneous dynamic pressure). At the advance ratio of 1.0, the lift plateaus and approaches zero during the middle of the retreating phase.

Surging - Flow Field

In Figure 5, the instantaneous vorticity magnitude is presented for the case with advance ratio of 0.5 at 4 different phases of the cycle. Flow is turbulent and is attached for most of the oscillation cycle. Comparing the flow during the advancing phase (Figures 5a and 5b) to the flow in the retreating phase (Figures 5c and 5d), it can be seen that the boundary layer is thinner with fewer vortical structures in the wake during the the advancing phase. This is due to the higher instantaneous Reynolds number during the advancing phase. However, when comparing the flowfield at $\tilde{t}$=0.13 with $\tilde{t}$=0.38 or $\tilde{t}$=0.63 with $\tilde{t}$=0.88, it is not the same despite being at comparable instantaneous Reynolds number. When the airfoil has positive acceleration (i.e., at $\tilde{t}$=0.13 and $\tilde{t}$=0.88) there are less vortical structures around the airfoil than when it is decelerating (i.e., at $\tilde{t}$=0.38 and $\tilde{t}$=0.63). Additionally, at phase $\tilde{t}$=0.88 there is marginal separation near the trailing edge over the pressure or lower side, which is not present at $\tilde{t}$=0.63. The normalized lift is fairly comparable when comparing these selected phases (see Figure 4).

At the higher advance ratio of 1.0, the flow is turbulent as well and is attached for most of the oscillation cycle, see Figure 6. The amplitude of displacement is greater and results in larger deviation of Reynolds number from the mean. Comparing the flow at $\tilde{t}$=0.13, see Figures 5a and 6a, the boundary is thinner at the higher advance ratio, as expected due to the higher instantaneous Reynolds Number. When the airfoil retreats, vorticity accumulates around the airfoil and rolls up into a distinct vortex near the leading edge over the suction or upper side of the airfoil, shown in Figure 6c. This leading-edge vortex is ejected into the outer flow and advects downstream. The flow on the suction or upper side reattaches as the leading-edge vortex passes over the airfoil. Flow separation is also present

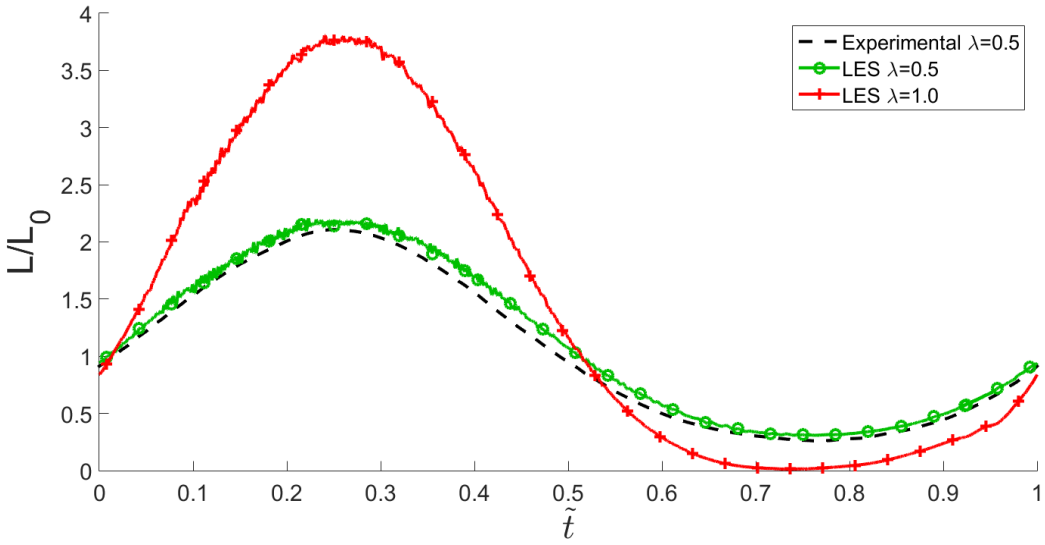

Fig. 4: Normalized lift for surging cases at λ=0.5 and 1.0

on the pressure or lower side of the airfoil during the retreating phase around $\tilde{t}$=0.67.

Pitching - Force Response Coefficient of lift, C_L, is shown in Figure 7. In this figure, LES and URANS predictions are compared to the phase averaged experimental data at a mean incidence angle of 10° with an amplitude of 10°. Recall that this case is also simulated using the unsteady Reynolds Averaged Navier Stokes (URANS) apporach, in which the Spalart-Allmaras turbulence model is employed. The LES and URANS datasets are instantaneous in nature (i.e., taken over a single cycle) and therefore, exhibits fine-scale fluctuations due to the presence of a turbulent flow over the airfoil; phase-averaged data from simulations will be considered in the future. Again, simulations are carried out for up to three oscillation cycles and data is presented from the last cycle.

Overall, there is a reasonable agreement in the trend of the force response, however, there seems to be a difference in fluctuation level as well as phase (i.e., a phase lag is present) between the experimental data and simulations predictions (from both LES and URANS). As the airfoil pitches up, lift increases until the airfoil stalls and is followed by a large fluctuation in the lift due to the shedding of the primary vortex. This part of the pitching cycle is labeled as part A. Secondary and tertiary vortices form and shed later in the pitching cycle, resulting in more fluctuations in the lift. This is clear in the next three parts B, C and D of the pitching cycle. These three parts are defined between $\tilde{t}$=0.2 and 0.75 due to the presence of three local peaks and valleys in the lift force during this portion of the pitching cycle. The primary flow features such as flow separation, vortex shedding and flow reattachment are predicted by LES, though LES predicts a stronger or higher fluctuation in the lift force in parts A, B and C of the pitching cycle as compared to the experimental data, while a lower fluctuation in part D. Further, LES predictions show a phase lag. URANS predictions match better in part A of the cycle, however, in other parts of the cycle does not capture the trend in the lift force and misses prominent features. Specifically in part D (between $\tilde{t}$=0.45 and 0.75), the local peak is lacking in the URANS data as compared to the experimental data. URANS predictions also show a phase lag. To remove phase lag in LES and URANS datasets, the simulation data is shifted such that it matches with the experimental data at the beginning of the cycle, i.e., at $\tilde{t}$=0 or ϕ=0°. Shifted simulation datasets are compared with the experimental data in Figure 8. The overall observations are similar in that the LES predictions better capture the prominent features in the lift force response.

Pitching - Flow Field The flowfield predicted by LES is shown in Figure 9 at 8 different phases of the cycle. Over the cycle, there are large-scale vorticies that are formed and shed. Figure 9a shows instantaneous vorticity at $\tilde{t}$=0.13 when the primary vortex is fully formed. Note that the flow is separated over the entire airfoil (i.e., on the suction or upper side). Once this vortex advects downstream, a massive flow separation is present over the airfoil (e.g., see Figure 9b at $\tilde{t}$=0.21). While the flow is separated, as shown in the force response, (large-scale) secondary and tertiary vortices form and shed. Figures 9c through 9f show these vortices. As the airfoil pitches down, the flow begins to reattach over the suction side, e.g., see Figures 9e and 9f. By $\tilde{t}$=0.63, the flow is completely reattached on suction or upper side as shown in Figure 9g, while it is still separated on the pressure or lower side towards the trailing edge. By $\tilde{t}$=0.71, shown in Figure 9h, the flow is attached on both sides of the airfoil, which is expected due to low incidence angle.

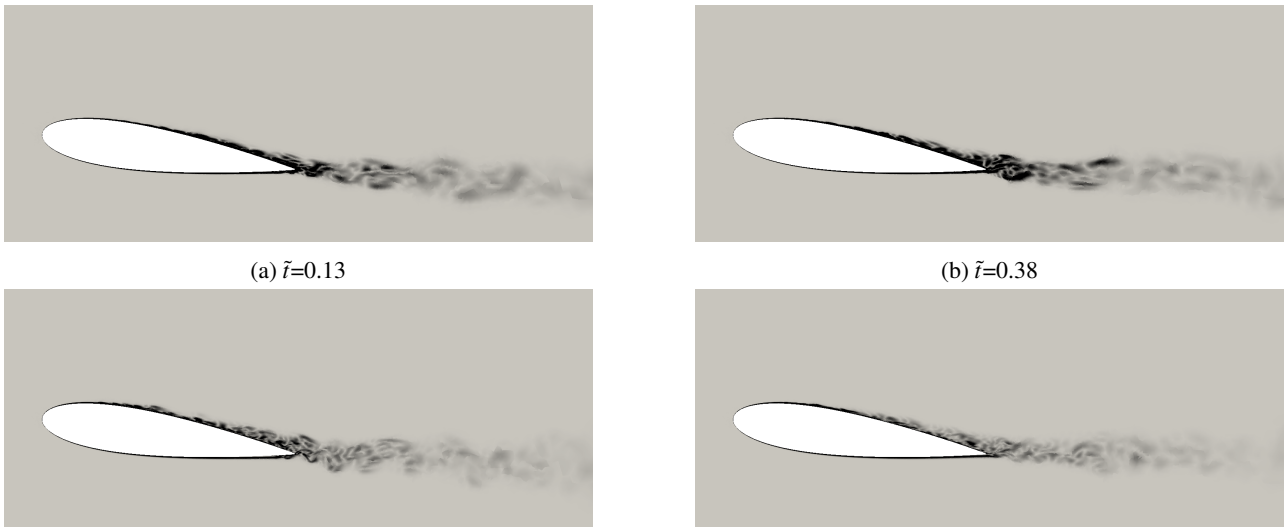

(a) $\tilde{t}$=0.13 (b) $\tilde{t}$=0.38

(c) $\tilde{t}$=0.63 (d) $\tilde{t}$=0.88

Fig. 5: Vorticity magnitude for surging case at λ =0.5, maximum value (darkest color) is set to $60U_\infty/C$

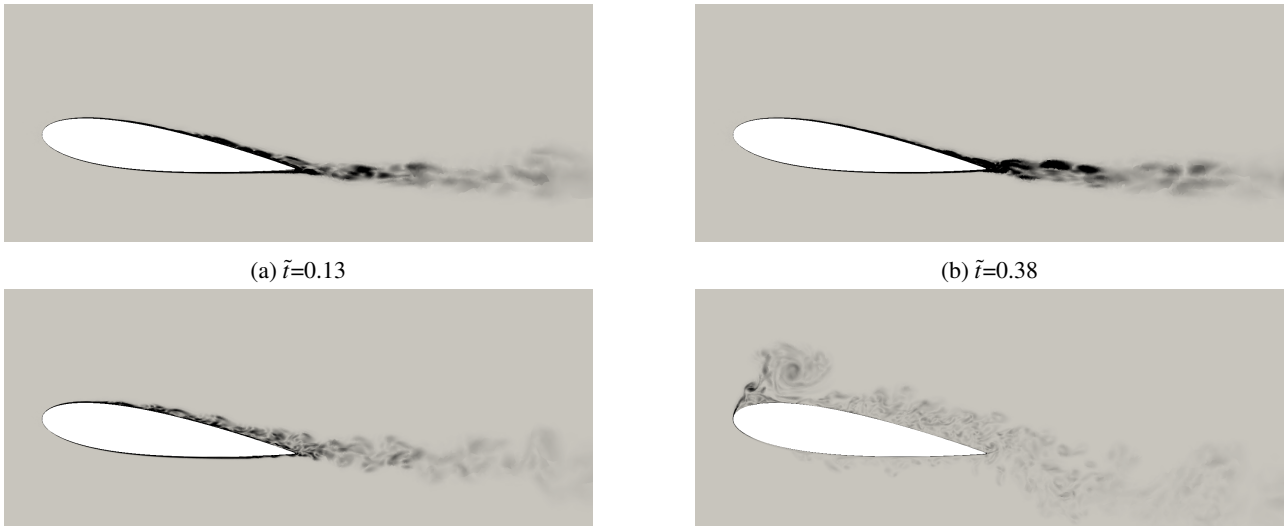

(a) $\tilde{t}$=0.13 (b) $\tilde{t}$=0.38

(c) $\tilde{t}$=0.63 (d) $\tilde{t}$=0.88

Fig. 6: Vorticity magnitude for surging case at λ =1.0, maximum value (darkest color) is set to $60U_\infty/C$

CLOSING REMARKS

A dynamic large eddy simulation (LES) based numerical investigation was carried out for flow over an oscillating airfoil. Two sets of cases were considered. One set of cases considered an airfoil with moderate to large streamwise oscillations while the other considered an airfoil with a large pitching motion.

For the surging airfoil, the airfoil was subjected to a sinusoidal surging motion at a fixed incidence angle in a constant freestream flow. LES predictions of the lift response at the moderate advance ratio of λ=0.5 were compared to the wind tunnel experiments of Strangfeld et al. 26 and showed a good agreement. Predictions were also made for a surging airfoil at λ=1.0. The flowfield was analyzed for both cases. For both advance ratios, it was found that the boundary layer is thinner and has less vortical structures in the wake during the advancing phase than in the retreating phase. When the airfoil retreats, vorticity accumulates around the airfoil and at λ=1.0 a roll up of a distinct leading-edge vortex over the suction side was observed.

For the pitching airfoil, the airfoil was subjected to a sinusoidal pitching motion in a constant freestream flow. The airfoil was set a mean incidence of 10° and an amplitude of 10°. In this case, LES and unsteady Reynolds-averaged Navier-Stokes (URANS) predictions were compared to the experimental data. LES was able to predict the overall trend in the force response and better captured the prominent features, whereas the URANS missed several prominent features. A phase lag was observed in both LES and URANS force data

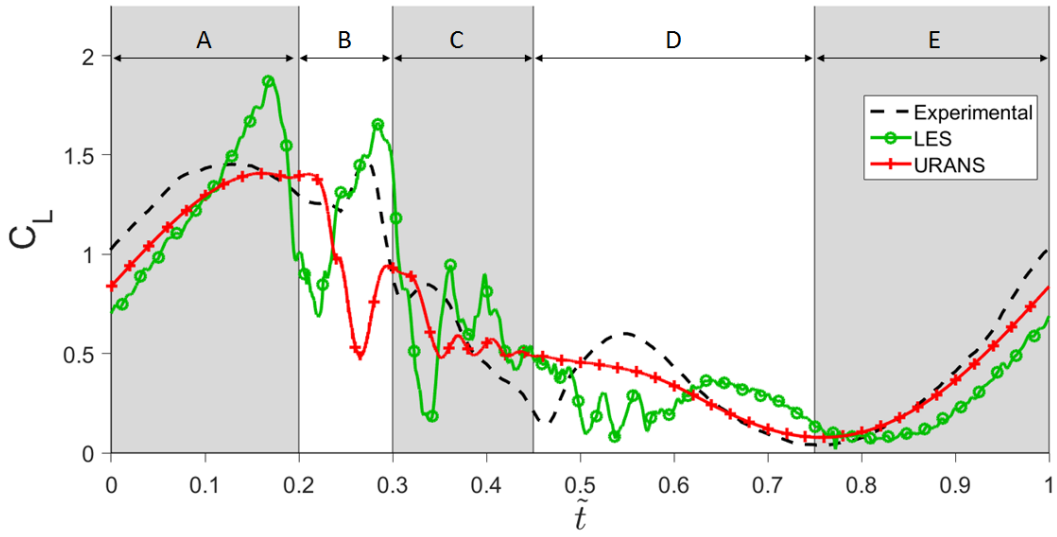

Fig. 7: Coefficient of lift for pitching case

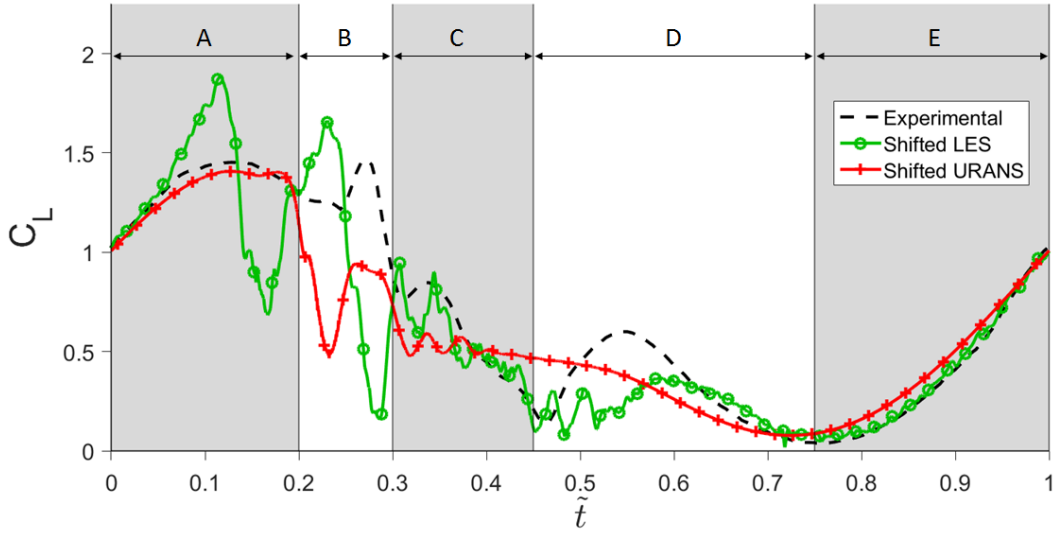

Fig. 8: Coefficient of lift for pitching case with a phase shift applied to LES and URANS data

as compared to experimental data. Flowfield was analyzed at different phases showing formation and shedding of multiple large-scale vortices over the pitching cycle.

Author contact:
Alexander Kocher: kochea@rpi.edu
Reed Cummings: rcumming557@gmail.com
Onkar Sahni: sahni@rpi.edu

ACKNOWLEDGMENTS

We would like to acknowledge that the computational resources used in this study were provided by Rensselaer's Center for Computational Innovations (CCI). We would also like to acknowledge that meshing software was provided by Simmetrix, Inc. URANS simulations were carried out by using the AcuSolve^{TM} software, provided by Altair Engineering, Inc. We would also like to acknowledge the help of Drs. D. Greenblatt, H. Mueller-Vahl and C. Strangfeld with the experimental data. This research was funded in part by National Science Foundation's CAREER grant 1350454 and by the Department of Energy, Office of Science's SciDAC-III Institute as part of the Frameworks, Algorithms, and Scalable Technologies for Mathematics (FASTMath) program under grant DE-SC0006617.

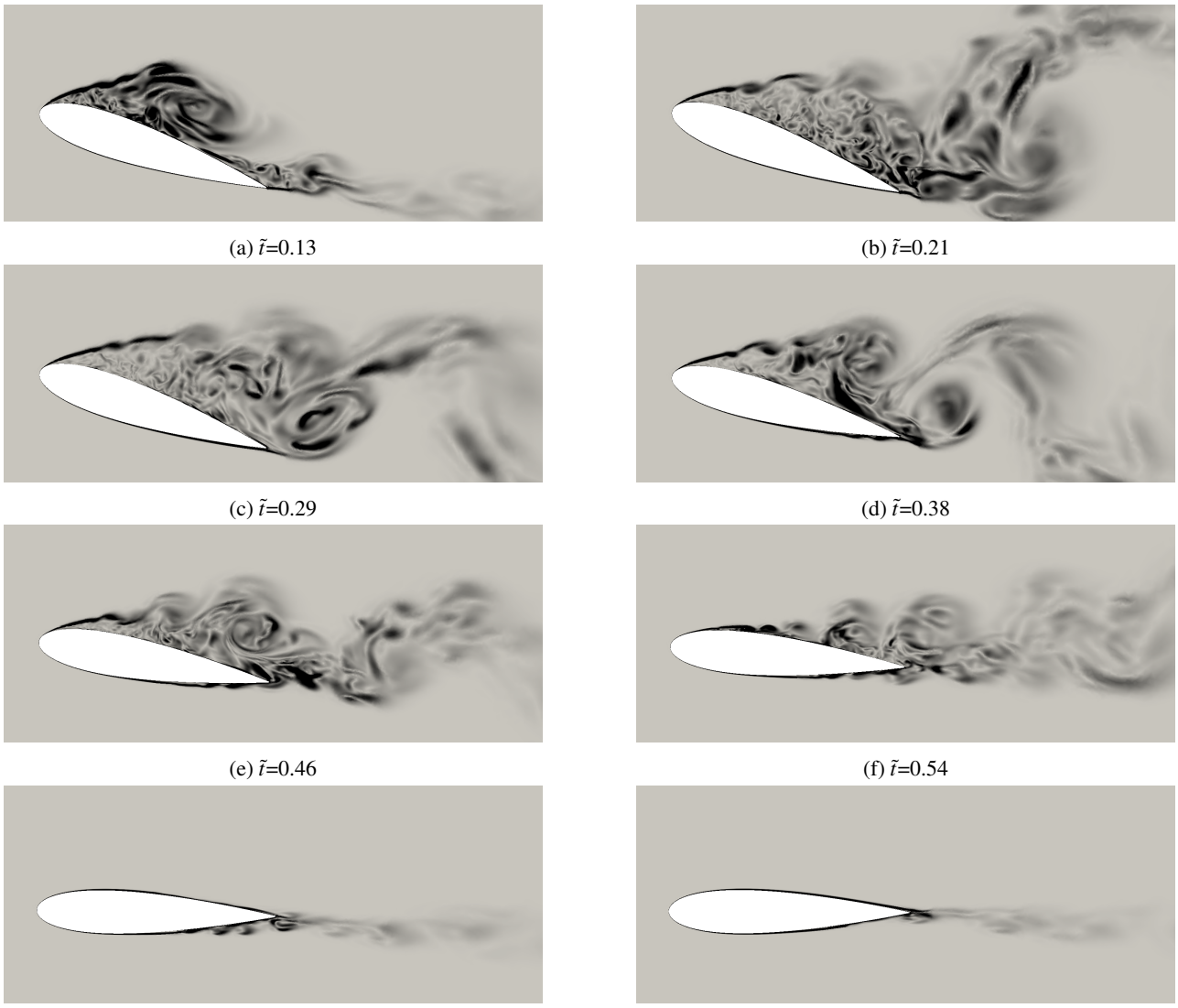

(a) $\tilde{t}$=0.13 (b) $\tilde{t}$=0.21

(c) $\tilde{t}$=0.29 (d) $\tilde{t}$=0.38

(e) $\tilde{t}$=0.46 (f) $\tilde{t}$=0.54

(g) $\tilde{t}$=0.63 (h) $\tilde{t}$=0.71

Fig. 9: Vorticity magnitude for pitching case, maximum value (darkest color) is set to $60U_\infty/C$

REFERENCES

[1]Greenblatt, D., Mueller-Vahl, H., Strangfeld, C., Ol, M. V., and Granlund, K. O.54th AIAA Aerospace Sciences Meeting, AIAA Paper 2016-1356, 2016.

[2]Granlund, K. O., Ol, M. V., and Jones, A. R.*AIAA Journal*, Vol. 54, (5), 2016, pp. 1628–1636.

[3]Visbal, M. R.52nd Aerospace Sciences Meeting, AIAA Paper 2016-0591, 2014.

[4]Gross, A. and Wen, G.8th AIAA Flow Control Conference, AIAA Paper 2016-4244, 2016.

[5]Stangfeld, C., Rumsey, C. L., Mueller-Vahl, H., Greenblatt, D., Nayeri, C., and Paschereit, C. O.45th AIAA Fluid Dynamics Conference, 2015.

[6]Hodara, J., Lind, A. H., Jones, A. R., and Smith, M. J.*Journal of the American Helicopter Society*, Vol. 61, (3), 2016, pp. 1–15.

[7]Norman, T. R., Shinoda, P., Peterson, R. L., and Datta, A.American Helicopter Society 67th Annual Forum, 2011.

[8]Chaderjian, N. M. and Ahmad, J. U., 2012.

[9]Potsdam, M., Datta, A., and Jayaraman, B.*Journal of the American Helicopter Society*, Vol. 61, (2), 2016, pp. 1–17.

[10]Tran, S., Cummings, R., and Sahni, O.*Computers & Fluids*, (in print), http://dx.doi.org/10.1016/j.compfluid.2016.10.027.

[11]Tran, S. and Sahni, O.*Journal of Turbulence*, (in print), http://dx.doi.org/10.1080/14685248.2017.1280607.

[12]Sahni, O., Jansen, K. E., Shephard, M. S., Taylor, C. A.,

and Beall, M. W.*Engineering with Computers*, Vol. 24, (3), 2008, pp. 267–285.

[13]Rodriguez, J. M., Sahni, O., Lahey, R. T., and Jansen, K. E.*Computers & Fluids*, Vol. 87, 2013, pp. 115–131.

[14]Sahni, O., Ovcharenko, A., Chitale, K. C., Jansen, K. E., and Shephard, M. S.*Engineering with Computers*, (in print), http://dx.doi.org/10.1007/s00366-016-0437-2.

[15]Sahni, O., Luo, X., Jansen, K., and Shephard, M.*Finite Elements in Analysis and Design*, Vol. 46, (1), 2010, pp. 132–139.

[16]Zhang, A. and Sahni, O.54th AIAA Aerospace Sciences Meeting, AIAA Paper 2016-1099, 2016.

[17]Sahni, O., Zhou, M., Shephard, M. S., and Jansen, K. E.Proceedings of the Conference on High Performance Computing Networking, Storage and Analysis, 2009.

[18]Sahni, O., Carothers, C. D., Shephard, M. S., and Jansen, K. E.*Scientific Programming*, Vol. 17, (3), 2009, pp. 261–274.

[19]Zhou, M., Sahni, O., Kim, H. J., Figueroa, C. A., Taylor, C. A., Shephard, M. S., and Jansen, K. E.*Computational Mechanics*, Vol. 46, (1), 2010, pp. 71–82.

[20]Tran, S. and Sahni, O.54th AIAA Aerospace Sciences Meeting, AIAA Paper 2016-0341, 2016.

[21]Cummings, R., Tran, S., and Sahni, O.Proc. 8th International Colloquium on Bluff Body Aerodynamics and Applications, 2016.

[22]Wang, Z. and Oberai, A. A.*Physics of Fluids*, Vol. 22, (7), 2010, pp. 075107.

[23]Hughes, T. J. and Sangalli, G.*SIAM Journal on Numerical Analysis*, Vol. 45, (2), 2007, pp. 539–557.

[24]Oberai, A. and Wanderer, J.*Journal of Turbulence*, Vol. 6, 2005, pp. N7.

[25]Meneveau, C., Lund, T. S., and Cabot, W. H.*Journal of Fluid Mechanics*, Vol. 319, 1996, pp. 353–385.

[26]Strangfeld, C., Müller-Vahl, H., Nayeri, C., Paschereit, C., and Greenblatt, D.*Journal of Fluid Mechanics*, Vol. 793, 2016, pp. 79–108.

[27]Müller-Vahl, H. F., *Wind turbine blade dynamic stall and its control*, Ph.D. thesis, TU Berlin, Technion Haifa, August 2015.